Recent progress in 2D group-V elemental monolayers: fabrications and properties

Peiwen Yuan, Teng Zhang, Jiatao Sun, Liwei Liu†, Yugui Yao, and Yeliang Wang

MIIT Key Laboratory for Low-Dimensional Quantum Structure and Devices, Beijing Institute of Technology, Beijing 100081, China

Abstract: A large number of two-dimensional (2D) monoelemental materials with huge application potentials have been developed, since graphene was reported as a monoelemental material with unique properties. As cousins of graphene, 2D group-V elemental monolayers have gained tremendous interest due to their electronic properties with significant fundamental bandgap. In this review, we extensively summarize the latest theoretical and experimental progress in group-V monoelemental materials, including the latest fabrication methods, the properties and potential applications of these 2D monoelementals. We also give a perspective of the challenges and opportunities of 2D monoelemental group-V monolayer materials and related functional nanodevices.

Key words: 2D materials; group-V monolayer; phosphorene; arsenene; antimonene; bismuthene

1. Introduction

Two-dimensional (2D) materials are a kind of monolayer or fewer layer materials whose thickness is much smaller than the lateral dimension. Many of them have novel electronic[1–4] and optoelectronic properties[5–7], such as, the quantum-confined electronic band structures[8], layer-dependent bandgaps[9], and atom-lattice-related conductance transition from semiconductors to metals[10] As a classic 2D material, graphene has excellent electron mobility with excellent performance in transistors and as electrochemical electrodes[11]. However, one weakness of the electronic structure of graphene, so are silicene and germanene, is the very small bandgap[12], which limits their applications in high-end electronic nanodevices.

Different from the small bandgap materials, 2D monolayers of group-V elements are semiconductors with significant fundamental bandgaps, which have unique and promising electrical transport properties[13], outstanding carrier mobilities[14], topological transmission states, and negative Poisson's ratio[15], rendering them great application potentials in the next-generation functional nanodevices. 2D group-V monolayer materials include phosphorene, arsenene, antimonene and bismuthene, consist of phosphorus, arsenic, antimony and bismuth (see Fig. 1), respectively. Among these group-V elemental monolayers, the first explored and extensively studied one is phosphorene. Significantly, phosphorene has a tunable bandgap from 1.51 eV for a black phosphorus monolayer to 2 eV for a blue phosphorus monolayer, which would make it ideal for applications in nanoelectronic devices[16–20]. Besides, two novel 2D wide-bandgap semiconductors, named as arsenene (monolayer As) and antimonene (monolayer Sb), were theoretically predicted[21]. Both of them

have significant bandgap with high stability, making them suitable for the optoelectronic devices. In addition, bismuthene, which is a monolayer of bismuth, has been found to be topologically nontrivial with a large spin-orbit-coupling gap[22, 23].

This review will sum up the latest progress on 2D group-V materials (phosphorene, arsenene, antimonene and bismuthene), especially the fabrication of group-V monolayers and their fundamental properties and applications. Finally, we will give a perspective on 2D group-V elemental semiconductors.

2. Fabrications and electronic structures of group-V monolayers

2.1. Phosphorene

As a popular element in the Elemental Period Table, phosphorus has white, red, black and several other amorphous forms[24–26]. Among all the amorphous forms of phosphorus, black phosphorus (BP) is the most studied and stable allotrope, which has a strong in-plane covalent bonding network with sp^3-hybridized phosphorus atoms covalently bonded and weak van der Waals interactions between individual layers[27], as shown in Fig. 2(a). The unique structural arrangement endows BP with amounts of novel properties, such as the tunable band gap from 0.3 eV for bulk BP to ~2 eV for monolayer BP[28, 29] (Figs. 2(b) and 2(c)), moderate on/off ratio and high charge carrier mobility, which makes it ideal for the applications in field effect transistors[30], optoelectronics, photodetectors[31] and other devices. Since the discovery of layered 2D BP in 2014[32], there have been more and more theoretical and experimental research on layered 2D BP. More recently, Baboukani *et al.* fabricated high-quality and orthorhombic crystal structured phosphorene through electrochemical exfoliation in deionized (DI) water, where BP power, stainless steel and DI water served as the raw material, electrode, and electrolyte respectively[33]. The SEM and TEM images of BP nanosheets are shown in Figs. 2(d)–2(f).

Fig. 1. (Color online) Group-V elements in the period table. Among group-V elements, phosphorus, arsenic, antimony and bismuth (highlighted by blue-frame) are contributed to the formation of 2D monolayer materials phosphorene, arsenene, antimonene and bismuthene, respectively.

Blue phosphorus, which was first introduced as "phosphorene"[34], is 2D counterpart of black phosphorus. However, the structure of blue phosphorene has slightly flatter "zigzag" ridges rather than the deeper "armchair" ridges of black phosphorus[35–38], as shown in Figs. 2(a) and 2(e). The first realization in experiment of large-scale 2D blue phosphorus was on a Au(111) substrate by molecular beam epitaxy (MBE) in 2016[39]. The main preparation steps are as follows: First, phosphorus was evaporated from the crucible containing bulk black phosphorus at 260 °C, and then was deposited on a clean Au(111) surface for 3 min, which was heated at 230 °C. Finally, the substrate containing deposited phosphorus was annealed at 250 °C for 60 min. In this way, single layer phosphorus on Au(111) was successfully fabricated, as shown by STM image in Fig. 2(j). The high-resolution STM image and the corresponding line-profile (Fig. 2(j)) revealed a well-ordered hexagonal appearance of monolayer blue phosphorus. Interestingly, the product on the substrate, is blue phosphorus rather than black phosphorus. The main reason is probably due to the lattice mismatch between the black phosphorus and the substrate surface. This fabrication method of high-quality and large-scale single-layer blue phosphorus would be extended to many other 2D materials, which is hard to be achieved for large quantity by mechanical exfoliation. Moreover, Wang et al. reported the single vacancy (SV) defects could create mid-gap states within the fundamental bandgap of blue phosphorene[40], as shown in Fig. 2(j) — perfect blue phosphorene with the bandgap of 1.94 eV and Fig. 2(k) — SV-(5|9) in blue phosphorene with the bandgap of 1.38 eV. In particular, SV-(5|9) in blue phosphorene shows considerable spin densities around the defect, as shown in Fig. 2(l), which paves a way for the application in blue phosphorene-based spintronics.

2.2. Arsenene

The metallic feature of multilayered arsenic is preserved until the thickness is decreased to a bilayer with a bandgap of 0.37eV, and to monolayer arsenene with a wide bandgap of 2.49 eV, predicted from density-function-theory (DFT) calculations in 2015[21]. Theoretically, monolayer arsenene prefers a buckled honeycomb structure (Figs. 3(a) and 3(b)), instead of puckered and planar structure which are less favorable energetically[21, 43]. In addition, external strain has been studied not only to turn indirect semiconductor arsenene into a direct band-gap semiconductor and semi-metal, as shown in Fig. 3(c), but also as a way to transform arsenene to a topological insulator, which has a quantum spin Hall state[41]. Furthermore, Pizzi et al. in 2016 theoretically reported that arsenene was viewed as a promising 2D material for field effect transistors, which could apply in future nanoelectronics[44].

So far, although the synthesis of buckled arsenene with monolayer thickness has not reported experimentally, a large amount of efforts has been paid to fabricate arsenene sheet in experiment. In 2017, Tsai et al. fabricated multilayer arsenene on InAs by the plasma-assisted method[45], but its polycrystalline characteristics on the semiconductor substrate is not benefit for the study of its electrical properties.

Besides the plasma-assisted method, it has been recently reported that a high-yield arsenic nanosheets can be prepared by the method of aqueous shear exfoliation[42]. Among the allotropes of arsenic, the most stable form is gray arsenic, which has the rhombohedral layered structure, making it very brittle and can be easily pulverized. The gray arsenic are used to fabricate arsenic nanosheets by the method of aqueous shear exfoliation. The fabrication process mainly contains three steps. The first step is the pre-treatment step, purifying the powders to remove oxides on bulk arsenic crystal surface. The starting materials (arsenic powder) were initially sonicated in aqueous surfactant sodium cholate (SC) in an ice bath. The suspensions were centrifuged, the powders were then dried at 60 °C in a vacuum oven. In the second step, the pre-treated powders were submitted in aqueous surfactant SC for shear dispersion and exfoliation by two types of kitchen-like blenders, i.e., a bottom shear mixer and a top shear mixer alternatively. In the process of shear exfoliation, use the bottom mixing in counter-clockwise and the top mixing in clockwise. In the third step, the suspensions were first centrifuged. Finally, the arsenic nanosheets were separated by aqueous washing and centrifugation at different rotation speed, and were dried at 60 °C in vacuum for follow-up studies.

Figs. 3(d) and 3(e) show the comparison between the starting materials and the final product of the shear exfoliation process. By using transmission electron microscope (TEM), the morphology of exfoliated arsenic nanosheets were shown in Fig. 3(f). The achieved arsenic nanosheets has visible wrinkled structure, which consists of few-layer materials. In addition, using the dynamic light scattering, the particles with diameters of arsenic nanosheets was investigated, which ranges between 100–200 nm dominantly.

2.3. Antimonene

2.3.1. Epitaxial growth of buckled monolayer antimonene

Antimonene, which was predicted to have a bandgap of 2.28 eV[21], has got more and more attention recently. This significant bandgap of antimonene implies its promising
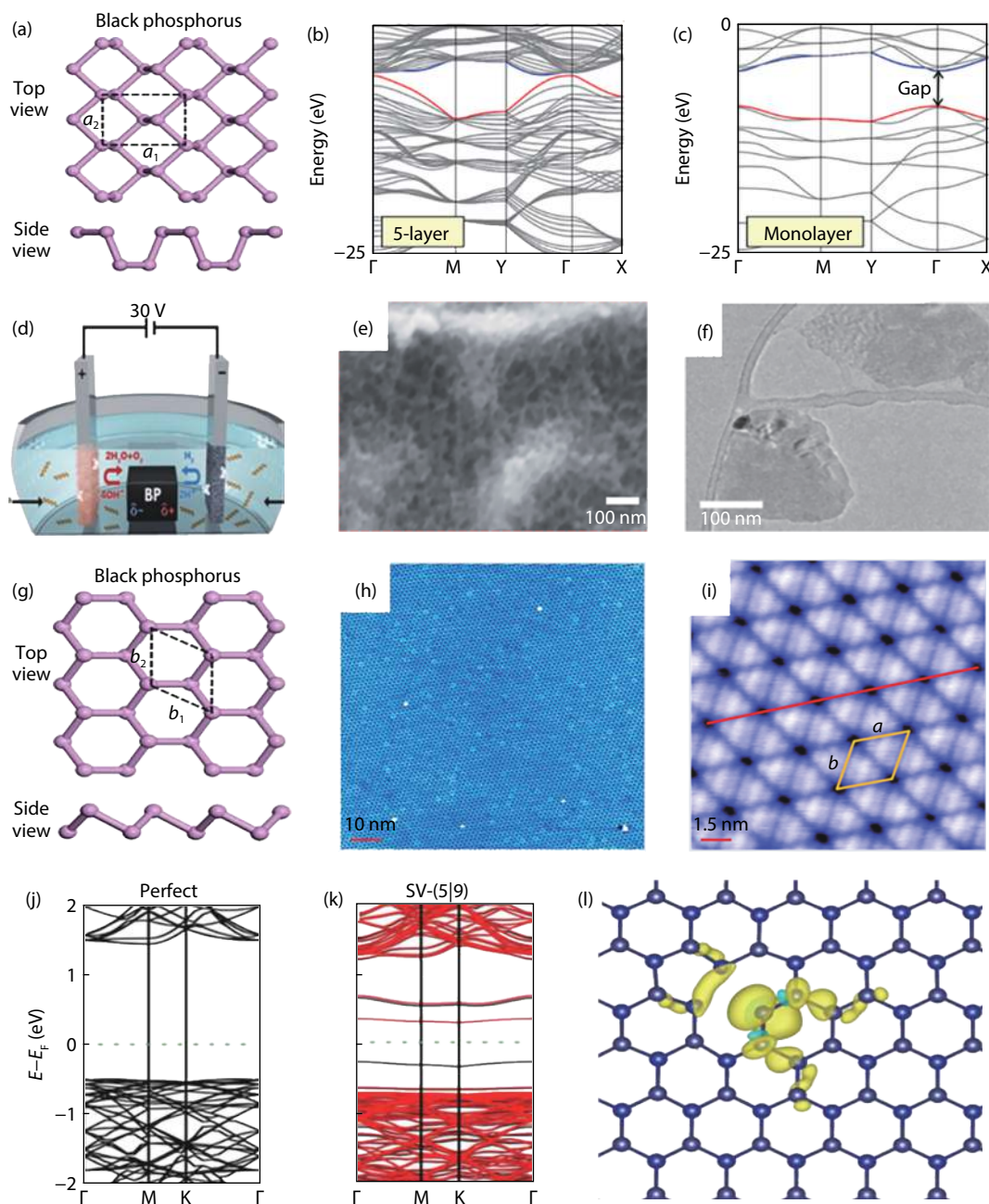
Fig. 2. (Color online) (a) The atomic structures of monolayer black phosphorus (BP). The unit cells are highlighted by the black rectangle. a_1 and a_2 represent the armchair edge and zigzag edge, respectively. (b, c) Electronic band dispersion of monolayer and five-layer BP, respectively. (d) Schematic illustration of preparing BP nanoparticles in water. (e) TEM image of BP nanosheets. (f) SEM images of exfoliated and deposited BP nanosheets. (g) The atomic structures of monolayer blue phosphorus. (h, i) Large-scale and high-resolution STM images of single layer phosphorus on Au(111), respectively. The unit cell in (i) is highlighted by yellow rhombus. (j, k) Calculated band structures of the perfect and spin-polarized SV-(5|9) defective blue phosphorene, respectively. (l) Spin density distribution for SV-(5|9). The yellow and blue colors represent the majority (positive) and the minority (negative) densities, respectively. (a, g–i) reproduced from Ref. [39] from American Chemical Society, copyright 2016; (b, c) reproduced from Ref. [28] from Scientific Citation Index, copyright 2015. (d–f) reproduced from Ref. [33] from Royal Society of Chemistry, copyright 2019. (j–l) reproduced from Ref. [40] from Scientific Citation Index, copyright 2020.

electronic and optoelectronics properties, which can be applied in optoelectronic devices. Recent studies have shown the fabrication of a few layers antimonene, but it is still difficult to grow high-quality monolayer antimonene[46, 47]. Large-scale and high-quality buckled monolayer antimonene was achieved on a PdTe$_2$ substrate by MBE method[48], which provides an effective way to achieve high-quality 2D materials.

The fabrication process of monolayer antimonene is illustrated in Fig. 4(a). The antimony atoms were evaporated from a Knudsen crucible and deposited onto a pre-cleaved PdTe$_2$ substrate kept at 400 K. Fig. 4(b) is a typical topographic image of as-resulted antimonene in a large-scale with a well-ordered LEED pattern inset, showing the high quality of the antimonene adlayer on the PdTe$_2$ substrate. Fig. 4(c) is a high-resolution STM image of antimonene adlayer, demonstrating a graphene-like honeycomb lattice of the antimonene. In addition, a buckled configuration of this honey-
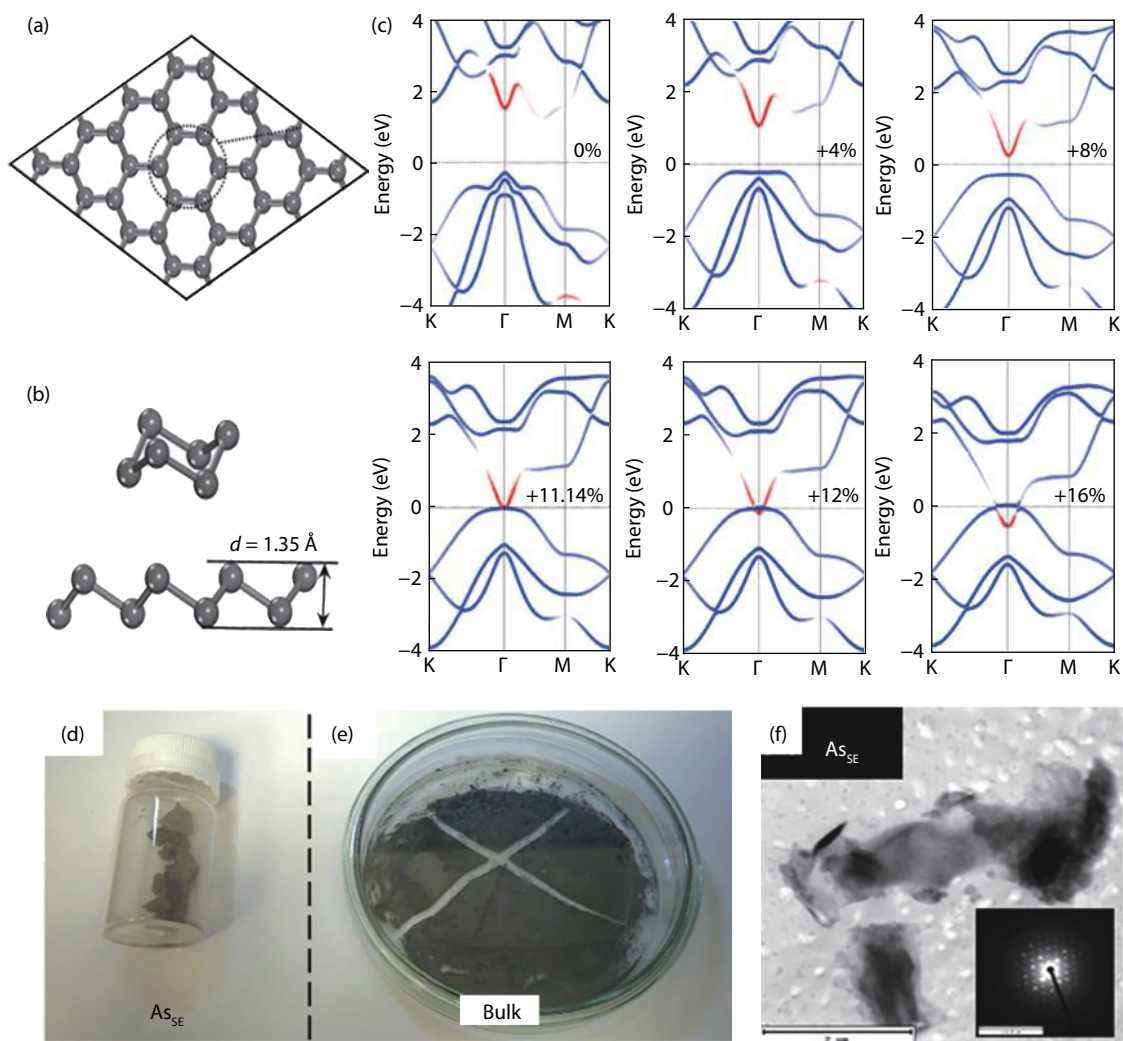
Fig. 3. (Color online) (a) Top view and (b) side view of a buckled As monolayer (arsenene). (c) The band structures of arsenene with respect to external tensile strain, while the red section denotes the contribution of s-type orbital and the blue section means the contribution of p-type orbital. (d, e) Visual comparison between final product of the aqueous shear exfoliation process (As_{SE}) and starting materials (bulk arsenic). (f) TEM image of shear-exfoliated arsenic nanosheets. (a, b) reproduced from Ref. [21] from Wiley, copyright 2015; (c) reproduced from Ref. [41] from Institute of Physics Publishing, copyright 2016; (d–f) reproduced from Ref. [42] from Wiley, copyright 2017.

comb lattice can be seen in Fig. 4(d). Moreover, the periodicity of this honeycomb lattice is 4.13 ± 0.02 Å, which is quite close to the lattice constant of the $PdTe_2$ substrate (4.10 ± 0.02 Å). Therefore, this close match of these two lattices consistent with the LEED pattern showing (1 × 1) diffraction points (inset in Fig. 4(b)). The apparent height of antimonene is 2.8 Å (Fig. 4(e)), showing that the antimonene adlayer is a monolayer. A relaxed model with calculated electron localization function (ELF) value of 0.6 is shown in Fig. 4(f), illustrating the continuity of the adlayer antimonene.

Fig. 4(g) is a cross-section ELF pattern perpendicular to the monolayer antimonene, which is corresponded to the black line in Fig. 4(f). This image clearly shows two important EFL ranges: the ELF value of the Sb–Sb pair is larger than 0.8 and the ELF value of the strongest coupling region between the antimonene and substrate is less than 0.3. The comparison of these EFL ranges demonstrates that a strong interaction exists within the antimonene and a weak interaction exists between antimonene and $PdTe_2$ substrate.

The environmental stability of atomic-thickness 2D materials is of great importance. STM images of the sample before and after exposed in the air were shown in Figs. 4(h) and 4(i), which reveal that the antimonene island are clean without any impurity on the islands. Moreover, after annealing the sample at 380 K, the STM image of antimonene island (Fig. 4(j)) is quite similar to the initial state image. This evidence strongly proves the monolayer antimonene is quite inert to air. More recently, topological edge states have been found in buckled antimonene islands on top of antimonene monolayers, which is promising for future low-power electronic nanodevices and quantum computations[49].

2.3.2.   Epitaxial growth of flat antimonene monolayer

Compared to monolayer graphene with flat honeycomb lattice, group-V monolayer materials usually have a buckled structure. Interestingly, flat antimonene monolayer (FAM) is theoretically predicted and also realized by MBE growth, as reported by Shao *et al.* in 2018[50]. FAM which inhibits hybridization between in-plane and out-of-plane orbitals, possess the quantum spin Hall effect, which would make them very suitable for applications in next-generation dissipationless electronic devices.

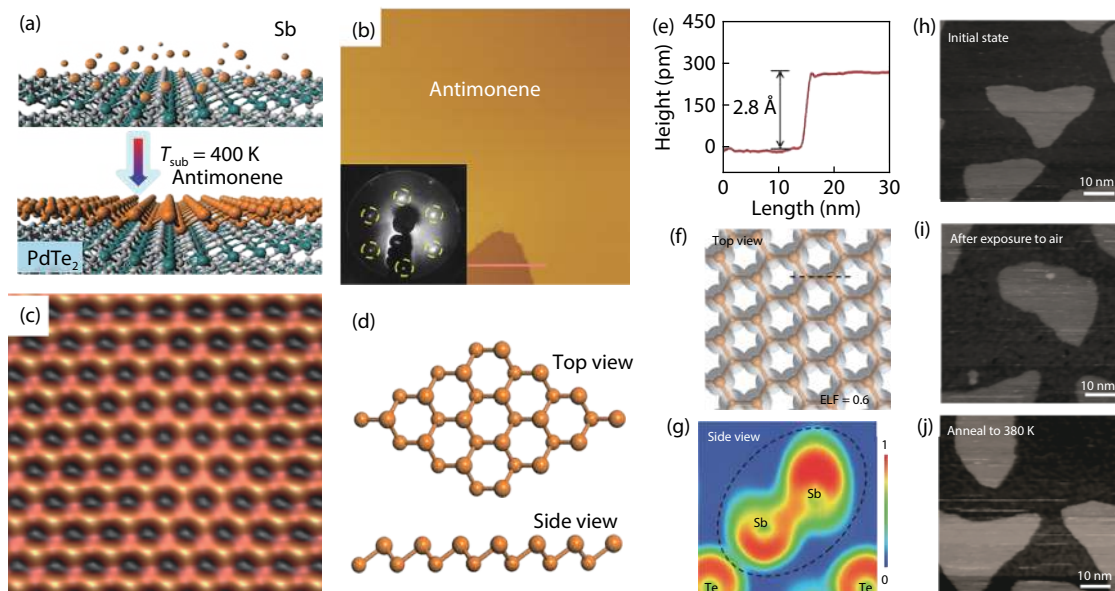Theoretically, the s-orbital and p-orbital projected band

Fig. 4. (Color online) (a) Schematic of fabrication process of buckled monolayer antimonene. (b) STM topographic image of large antimonene island on PdTe₂. Inset: LEED pattern of antimonene on PdTe₂. (c) Atomic resolution STM image of monolayer antimonene. (d) Top view (upper) and side view (lower) of the buckled antimonene. (e) A height profile, showing that the apparent height of the antimonene island. (f) Top view of the overall electron localization function (ELF) of the relaxed model, showing the continuity of the monolayer antimonene. (g) ELF of the cross section, demonstrating high localization of the electrons in Sb–Sb pairs. Typical STM image of antimonene islands on PdTe₂ substrate before air exposure in (h), after exposing to air for 20 min in (i), and after 380 K annealing in (j), respectively. Reproduced from Ref. [46]. Copyright 2017, Wiley.
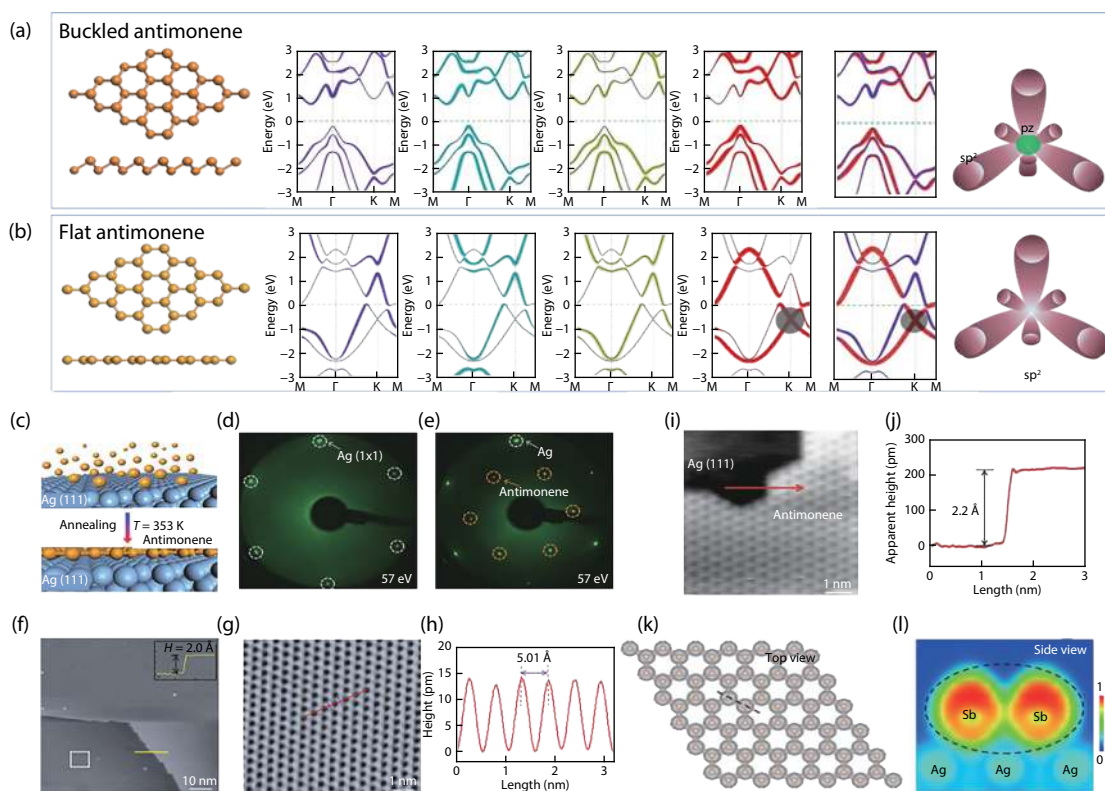

Fig. 5. (Color online) (a) Atomic structure and *s, p*-orbital projected band structure of buckled antimonene in (a) and flat antimonene in (b), in which the shade circles denote the Dirac cone from the out-of-plane *pz* orbitals. (c) Schematic of fabrication process of flat antimonene. LEED pattern of a clean Ag(111) substrate in (d) and antimonene film on Ag(111) in (e). (f) Large scale STM image of monolayer antimonene on the Ag(111). Inset: A height profile along the line at the terrace edge. (g) High-resolution STM image of antimonene. (h) Line profile revealing the periodicity of the antimonene lattice (5.01 Å). (i) A typical STM image of antimonene island on Ag(111). (j) The apparent height of the island. (k) Top view of the overall electron localization function (ELF) of the relaxed model of FAM. (l) Cross-sectional ELF along the black-dashed line in (k). Reproduced from Ref. [50] from American Chemical Society, copyright 2018.
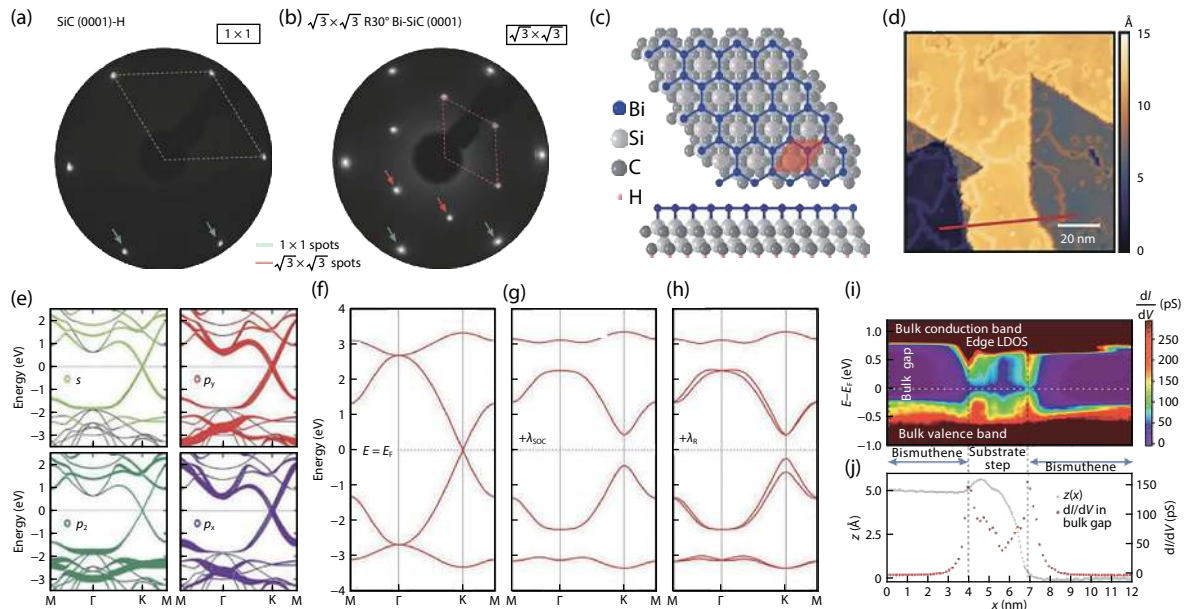
Fig. 6. (Color online) (a) LEED pattern of the SiC(0001)-H substrate, an unreconstructed (1 × 1) surface results from the hydrogenation of the top-layer Si dangling bonds. (b) After Bi deposition, ($\sqrt{3} \times \sqrt{3}$) R30° spots (red arrows) appears, indicating the formation of monolayer bismuthene on the surface. (c) Sketch of a bismuthene layer placed on the SiC(0001) substrate. (d) Topographic STM overview map showing that bismuthene fully covers the substrate. (e) The contribution of Bi s and p orbitals to the electronic structure of bismuthene (without SOC). (f) Electronic structure of the low-energy effective model without SOC. (g) Inclusion of the strong atomic SOC opens a huge gap at the K point. (h) Further including the Rashba term lifts the degeneracy of the topmost valence band and induces a large splitting with opposite spin character there. (i) Spatially resolved dI/dV data across the same step. The dI/dV signal of the in-gap states peaks at both film edges (gray dashed lines mark dI/dV maxima). (j) Topographic $z(x)$ line profile of the step and dI/dV signal of bismuthene (integrated over the gap from +0.15 to +0.55 eV), showing an exponential decrease away from the step edge, on either side. Reproduced from Ref. [53]. Copyright 2017, American Association for the Advancement of Science.

structure of the buckled antimonene are calculated, as shown in Fig. 5(a). The hybridized bands around the Fermi level between the s, p_x, p_y, p_z orbitals of the Sb atom lead to the partially hybridized sp^3 bands. As for the flat antimonene, there is no mutual hybridization between in-plane orbitals and out-of-plane ones as shown in Fig. 5(b). The in-plane orbitals lead to a hybridized sp^2 band. The out-of-plane orbitals lead to the Dirac cone of π bands resembling that of graphene around the Fermi level as denoted by the gray circles.

Experimentally, antimony atoms were deposited onto a pre-clean Ag(111) substrate kept at a relative low temperature of 353 K. A well-organized antimonene adlayer was formed on the substrate. Fig. 5(d) showed LEED pattern of the clean Ag(111) substrate with sharp (1 × 1) diffraction spots. Fig. 5(e) showed LEED pattern of the antimonene on the substrate, showing a ($\sqrt{3} \times \sqrt{3}$) R30° superstructure with respect to the Ag(111) surface lattice.

A typical STM image of the antimonene adlayer is shown in Fig. 5(f), revealing a uniform film on the substrate. Fig. 5(g) is the close-up STM image of the sample, showing a clear honeycomb-like lattice. Measured along the profile line in Fig. 5(g), the period of 5.01 Å for the antimonene was obtained, which is consistent with the superstructure observed in the LEED patterns. Moreover, the height of the antimonene film is 2.2 Å, as shown in Fig. 5(h), which is lower than the buckled monolayer antimonene (2.8 Å)[46], suggesting that the antimonene on the Ag(111) substrate has a lower buckling configuration. Based on first-principle calculations, the flat antimonene monolayer is the most energetic-

ally stable configuration on Ag(111) substrate, consistent with the experimental STM images.

Moreover, to determine whether Sb–Sb chemical bond exists in the flat configuration, the ELF of the antimonene monolayer on Ag(111) was carried out. Fig. 5(k) is the top view of the ELF for the optimized model of FAM, revealing the continuity of the antimonene. Along the black-line in Fig. 5(l) is the cross-sectional ELF, the different colors in different regions represent different interaction, suggesting strong chemical bond of the Sb-Sb pairs and weak Sb–Ag interaction. As for the configuration of this flat honeycomb lattice of FAM, it is sustained by the substrate. So, it is important to exfoliate these antimonene films from the substrate for its practical applications in the future, which need further exploring.

2.4. Bismuthene

Given antimonene with the bandgap of 2.28 eV[21], for bismuthene made of group-V elements, it is expected to have an even larger bandgap. Furthermore, as cousin of graphene, which was discovered with quantum spin Hall (QSH) effect, bismuthene has been particularly interested in search of the QSH state as it holds a similar honeycomb lattice with graphene[51]. Monolayer bismuthene has been predicted to be topologically nontrivial[22, 23, 52]. Therefore, realization of bismuthene as two-dimensional topological insulators is of great importance. Experimentally, a monolayer bismuthene with quantum spin Hall phase has been successfully realized on a SiC(0001) substrate by MBE method, as reported by Reis et al.[53].

In Reis's work, the use of SiC(0001) as the substrate is vi-

tal because this substrate is not only stabilizing the bismuthene as a quasi-2D topological insulator but also playing a great role in achieving a large gap. N-doped Si-terminated 4H-SiC substrate was first dry-etched in a hydro-based gas atmosphere at a temperature of ~1230 ℃. And then the H-termination of the substrate was removed by a slow thermal H desorption at ~650 ℃ while immediately offer Bi atoms on the substrate. The substrate was then lowered to ~500 ℃ to condense Bi layer, then a $\sqrt{3} \times \sqrt{3}$ R30° superstructure of Bi atoms with a honeycomb lattice reconstructed. Figs. 6(a) and 6(b) denoted a comparison of LEED patterns before and after the formation of monolayer bismuthene. Fig. 6(a) showed an unreconstructed (1 × 1) surface resulting from the hydrogenation of the top-layer Si dangling bonds on the SiC(0001) substrate. Fig. 6(b) showed ($\sqrt{3} \times \sqrt{3}$) R30° spots, indicating the formation of monolayer bismuthene on the surface after Bi deposition. Fig. 6(b) described schematically a bismuthene layer on the threefold-symmetric SiC(0001) substrate in ($\sqrt{3} \times \sqrt{3}$) R30° commensurate registry. Obviously, this configuration of the bismuthene is planar instead of buckled, due to the strain effect of the SiC substrate. The STM image (Fig. 6(d)) of the sample shows the bismuthene film is smoothly covered on the substrate. The bismuthene flakes are extended of ~25-nm, limited by domain boundaries.

To establish the electronic structure of the bismuthene material, Reis *et al.* decomposed the band structure into σ-bond contributions came from Bi 6s, p_x, p_y orbitals and π-bond contribution from p_z orbitals. The orbitals at low energy are mainly σ bands, as shown in Fig. 6(e), as the hybridization of bismuthene and substrate is via π bonds. Considering the electronic structure around E_F, for the low energy bands without spin-orbital coupling (SOC), there is a Dirac-like band crossing at the K point, as shown in Fig. 6(f). However, when considering a strong atomic SOC, there is a large bandgap at the K point (Fig. 6(g)), and the Rashba term λ_R can lift the degeneracy of the valence-band and induces the spin-degenerate of the conduction band at K point (Fig. 5(h)). By using scanning tunneling spectroscopy (STS), the differential tunneling conductivity (dI/dV) curves show that while the interior of the island shows insulating gap feature, conductive states exists at the edges (Figs. 6(i) and 6(j)), which suggests that QSH exists in bismuthene/SiC. More excitingly, the bulk gap of bismuthene is up to 0.8 eV, which makes it a candidate for a high-temperature quantum spin Hall material. Very recently, the strong interaction electrons at the edge of the bismuthene on SiC(0001) was also reported to exhibit Luttinger liquid feature, providing a new platform to study one-dimensional electronic feature[54].

3. Summary and perspectives

There has been enormous progress on the study of group-V monolayers, especially on the preparation of new members and structural tuning of new materials. Phosphorene, which has amounts of excellent properties, such as tunable direct gap, high carrier mobility has been successfully fabricated on a Au(111) substrate by MBE. Arsenic nanosheets have been successfully prepared by aqueous shear exfoliation, which has visible wrinkled structure consisting of few-layer materials. As for antimonene, high quality buckled antimonene monolayer has been successfully grown on a PdTe₂ substrate, which represented excellent air stability in ambient environment. Moreover, flat antimonene monolayer has been also successfully fabricated on a Ag (111) substrate by MBE, which holding tunable topological properties for future applications. Regarding bismuthene, flat configuration as a two-dimensional topological insulator (2DTI) was experimentally obtained on a SiC (0001) substrate, with a large SOC gap, making it a candidate for a high-temperature quantum spin Hall material.

Undoubtedly, the experimental realization of group-V monolayers extend the scope of 2D atomically-thick structure and pave a way for the future application in spintronics. However, there are still some drawbacks in above-mentioned works on 2D monoelemental group-V monolayer materials. (1) Until now, the synthesis of buckled arsenene with monolayer thickness, which was predicted theoretically a wide bandgap, is not reported experimentally. (2) The flat antimonene monolayer films by MBE method are not electrically isolated from the metal substrate. (3) The excited findings are that the intriguing topological properties of group-V monolayers are reported experimentally in both antimonene and bismuthene monolayer, however, the low-energy-cost devices, based on the topological property of group-V monolayer, are still lacking, although there reported a lot of optoelectronic devices utilizing the semiconductor properties. So, there are many opportunities for research to exploit the structural controlling and potential applications in functional nanodevices. We hope that this review will inspire more attempts and findings in the group-V families, and we believe that related challenges can be solved in the near future.

Acknowledgements

References

[1] Fiori G, Bonaccorso F, Iannaccone G, et al. Electronics based on two-dimensional materials. Nat Nanotechnol, 2014, 9, 768

[2] Novoselov K S, Mishchenko A, Carvalho A, et al. 2D materials and van der Waals heterostructures. Science, 2016, 353, aac9439

[3] Li G, Zhang Y Y, Guo H, et al. Epitaxial growth and physical properties of 2D materials beyond graphene: From monatomic materials to binary compounds. Chem Soc Rev, 2018, 47, 6073

[4] Gibertini M, Koperski M, Morpurgo A F, et al. Magnetic 2D materials and heterostructures. Nat Nanotechnol, 2019, 14, 408

[5] Cheng J B, Wang C L, Zou X M, et al. Recent advances in optoelectronic devices based on 2D materials and their heterostructures. Adv Opt Mater, 2019, 7, 1800441

[6] Epstein I, Chaves A J, Rhodes D A, et al. Highly confined in-plane propagating exciton-polaritons on monolayer semiconductors. 2D Mater, 2020, 7, 035031

[7] Kou J, Nguyen E P, Merkoçi A, et al. 2-dimensional materials-based electrical/optical platforms for smart on-off diagnostics applications. 2D Mater, 2020, 7, 032001

[8] Lin X, Lu J C, Shao Y, et al. Intrinsically patterned two-dimensional materials for selective adsorption of molecules and nano-

clusters. Nat Mater, 2017, 16, 717

[9] Niu X H, Yi Y W, Meng L J, et al. Two-dimensional phosphorene, arsenene, and antimonene quantum dots: Anomalous size-dependent behaviors of optical properties. J Phys Chem C, 2019, 123, 25775

[10] Zhang Y, Chang T R, Zhou B, et al. Direct observation of the transition from indirect to direct bandgap in atomically thin epitaxial MoSe$_2$. Nat Nanotechnol, 2014, 9, 111

[11] Das Sarma S, Adam S, Hwang E H, et al. Electronic transport in two-dimensional graphene. Rev Mod Phys, 2011, 83, 407

[12] Liu C C, Feng W X, Yao Y G. Quantum spin Hall effect in silicene and two-dimensional germanium. Phys Rev Lett, 2011, 107, 076802

[13] Wu Z H, Hao J H. Electrical transport properties in group-V elemental ultrathin 2D layers. npj 2D Mater Appl, 2020, 4, 4

[14] Zhang S L, Guo S Y, Chen Z F, et al. Recent progress in 2D group-VA semiconductors: From theory to experiment. Chem Soc Rev, 2018, 47, 982

[15] Qin G Z, Qin Z Z. Negative Poisson's ratio in two-dimensional honeycomb structures. npj Comput Mater, 2020, 6, 51

[16] Ma Y Q, Shen C F, Zhang A, et al. Black phosphorus field-effect transistors with work function tunable contacts. ACS Nano, 2017, 11, 7126

[17] Fei R X, Yang L. Strain-engineering the anisotropic electrical conductance of few-layer black phosphorus. Nano Lett, 2014, 14, 2884

[18] Liu Q, Zhang X W, Abdalla L, et al. Switching a normal insulator into a topological insulator via electric field with application to phosphorene. Nano Lett, 2015, 15, 1222

[19] Qiao J S, Kong X H, Hu Z X, et al. High-mobility transport anisotropy and linear dichroism in few-layer black phosphorus. Nat Commun, 2014, 5, 4475

[20] Phuong L T T, Phong T C, Yarmohammadi M. Spin-splitting effects on the interband optical conductivity and activity of phosphorene. Sci Rep, 2020, 10, 9201

[21] Zhang S L, Yan Z, Li Y F, et al. Atomically thin arsenene and antimonene: Semimetal-semiconductor and indirect-direct bandgap transitions. Angew Chem Int Ed, 2015, 54, 3112

[22] Wada M, Murakami S, Freimuth F, et al. Localized edge states in two-dimensional topological insulators: Ultrathin Bi films. Phys Rev B, 2011, 83, 121310

[23] Murakami S. Quantum spin Hall effect and enhanced magnetic response by spin-orbit coupling. Phys Rev Lett, 2006, 97, 236805

[24] Brown A, Rundqvist S. Refinement of the crystal structure of black phosphorus. Acta Crystallogr, 1965, 19, 684

[25] Thurn H, Kerbs H. Crystal structure of violet phosphorus. Angew Chem Int Ed, 1966, 5, 1047

[26] Hultgren R, Gingrich N S, Warren B E. The atomic distribution in red and black phosphorus and the crystal structure of black phosphorus. J Chem Phys, 1935, 3, 351

[27] Appalakondaiah S, Vaitheeswaran G, Lebègue S, et al. Effect of van der Waals interactions on the structural and elastic properties of black phosphorus. Phys Rev B, 2012, 86, 035105

[28] Fukuoka S, Taen T, Osada T. Electronic structure and the properties of phosphorene and few-layer black phosphorus. J Phys Soc Jpn, 2015, 84, 121004

[29] Liang L B, Wang J, Lin W Z, et al. Electronic bandgap and edge reconstruction in phosphorene materials. Nano Lett, 2014, 14, 6400

[30] Kim J S, Jeon P J, Lee J, et al. Dual gate black phosphorus field effect transistors on glass for NOR logic and organic light emitting diode switching. Nano Lett, 2015, 15, 5778

[31] Buscema M, Groenendijk D J, Blanter S I, et al. Fast and broadband photoresponse of few-layer black phosphorus field-effect transistors. Nano Lett, 2014, 14, 3347

[32] Li L K, Yu Y J, Ye G J, et al. Black phosphorus field-effect transistors. Nat Nanotechnol, 2014, 9, 372

[33] Baboukani A R, Khakpour I, Drozd V, et al. Single-step exfoliation of black phosphorus and deposition of phosphorene via bipolar electrochemistry for capacitive energy storage application. J Mater Chem, 2019, 7, 25548

[34] Liu H, Neal A T, Zhu Z, et al. Phosphorene: an unexplored 2D semiconductor with a high hole mobility. ACS Nano, 2014, 8, 4033

[35] Xie J, Si M, Yang D, et al. A theoretical study of blue phosphorene nanoribbons based on first-principles calculations. J Appl Phys, 2014, 116, 073704

[36] Aierken Y, Cakir D, Sevik C, et al. Thermal properties of black and blue phosphorenes from a first-principles quasiharmonic approach. Phys Rev B, 2015, 92, 081408

[37] Ghosh B, Nahas S, Bhowmick S, et al. Electric field induced gap modification in ultrathin blue phosphorus. Phys Rev B, 2015, 91, 115433

[38] Zhu Z, Tománek D. Semiconducting layered blue phosphorus: A computational study. Phys Rev Lett, 2014, 112, 176802

[39] Zhang J L, Zhao S T, Han C, et al. Epitaxial growth of single layer blue phosphorus: A new phase of two-dimensional phosphorus. Nano Lett, 2016, 16, 4903

[40] Wang C, You Y Z, Choi J H. First-principles study of defects in blue phosphorene. Mater Res Express, 2019, 7, 015005

[41] Wang Y P, Zhang C W, Ji W X, et al. Tunable quantum spin Hall effect via strain in two-dimensional arsenene monolayer. J Phys D, 2016, 49, 055305

[42] Gusmão R, Sofer Z, Bouša D, et al. Innentitelbild: pnictogen (As, Sb, Bi) nanosheets for electrochemical applications are produced by shear exfoliation using kitchen blenders. Angew Chem Int Ed, 2017, 129, 14510

[43] Kamal C, Ezawa M. Arsenene: Two-dimensional buckled and puckered honeycomb arsenic systems. Phys Rev B, 2015, 91, 085423

[44] Pizzi G, Gibertini M, Dib E, et al. Performance of arsenene and antimonene double-gate MOSFETs from first principles. Nat Commun, 2016, 7, 12585

[45] Tsai H, Wang S, Hsiao C, et al. Direct synthesis and practical bandgap estimation of multilayer arsenene nanoribbons. Chem Mater, 2016, 28, 425

[46] Ares P, Aguilar-Galindo F, Rodríguez-San-miguel D, et al. Mechanical isolation of highly stable antimonene under ambient conditions. Adv Mater, 2016, 28, 6332

[47] Ji J P, Song X F, Liu J Z, et al. Two-dimensional antimonene single crystals grown by van der Waals epitaxy. Nat Commun, 2016, 7, 13352

[48] Wu X, Shao Y, Liu H, et al. Epitaxial growth and air-stability of monolayer antimonene on PdTe$_2$. Adv Mater, 2017, 29, 1605407

[49] Zhu S, Shao Y, Wang E, et al. Evidence of topological edge states in buckled antimonene monolayers. Nano Lett, 2019, 19, 6323

[50] Shao Y, Liu Z L, Cheng C, et al. Epitaxial growth of flat antimonene monolayer: A new honeycomb analogue of graphene. Nano Lett, 2018, 18, 2133

[51] Zhao A D, Wang B. Two-dimensional graphene-like Xenes as potential topological materials. APL Mater, 2020, 8, 030701

[52] Liu Z, Liu C X, Wu Y S, et al. Stable nontrivial Z2 topology in ultrathin Bi (111) films: A first-principles study. Phys Rev Lett, 2011, 107, 136805

[53] Reis F, Li G, Dudy L, et al. Bismuthene on a SiC substrate: A candidate for a high-temperature quantum spin Hall material. Science, 2017, 357, 287

[54] Stühler R, Reis F, Müller T, et al. Tomonaga–Luttinger liquid in the edge channels of a quantum spin Hall insulator. Nat Phys, 2020, 16, 47